ELSEVIER

Contents lists available at ScienceDirect

# Journal of Power Sources

journal homepage: www.elsevier.com/locate/jpowsour





# LBM studies on oxygen bubble transport in porous transport layers and flow channel of proton exchange membrane water electrolyzers

Ziheng Ding<sup>a</sup>, Ruixin Li<sup>a</sup>, Kai H. Luo<sup>a,b,\*</sup>

- <sup>a</sup> Center for Combustion Energy, Department of Energy and Power Engineering, Key Laboratory for Thermal Science and Power Engineering of Ministry of Education, Low Carbon Energy and CCUS Research Center, Institute for Carbon Neutrality, Tsinghua University, 10084, Beijing, China
- <sup>b</sup> Department of Mechanical Engineering, University College London, Torrington Place, London, WC1E 7JE, UK

#### HIGHLIGHTS

- A 3D lattice Boltzmann model with free surface model is developed.
- A random bubble generation model is constructed to link with electrochemistry.
- The dynamic bubble evolution in the PTLs and flow channel is studied.
- The differences caused by spherical and fibrous PTLs are investigated.
- Different PTL properties are studied to understand oxygen transport.

#### ARTICLE INFO

#### Keywords:

Proton exchange water membrane electrolyzer Porous transport layer Lattice Boltzmann method simulation Bubble transport

#### ABSTRACT

The transport and management of oxygen bubbles significantly impact the performance of proton exchange membrane water electrolyzers (PEMWE). The 3D structures of sintered and fibrous porous transport layers (PTLs) were reconstructed using randomly distributed spherical particles and layer-by-layer generated cylindrical fibers, respectively. The two-phase flow dynamic behavior of oxygen in the PTL and flow channel with lateral velocity were simulated based on the lattice Boltzmann method with a free surface model. At the bottom of the computational domain, spherical bubbles were added at random positions at specified intervals, corresponding to different current densities. The effects of bubble generation time interval, contact angle, initial flow velocity, graded porosity and microporous layer structure are investigated. The similarities and differences between spherical and fibrous PTLs are analyzed in detail. The results demonstrate the feasibility and necessity of operating PEMWEs at high current densities. Hydrophilic PTLs facilitate the upward movement of oxygen bubbles, with an optimal contact angle range observed. Maximizing the flow channel velocity within laminar conditions promotes the lateral expulsion of bubbles. Compared to spherical PTLs, fibrous PTLs are more suitable for high current density operations. Reducing the porosity or decreasing the fiber diameter near the catalyst layer side can effectively minimize bubble accumulation.

# 1. Introduction

Achieving carbon neutrality goals urgently requires innovative developments driven by transformative energy technologies. Search and rational utilization of clean energy sources that do not produce carbon dioxide have proven to be one of the most effective approaches [1,2]. Hydrogen, a plentiful, green, low-carbon secondary energy source, plays a crucial role in this context. It can be used for seasonal energy storage,

as well as a fuel or chemical feedstock, with applications across transportation, industry, and construction. Hydrogen serves as a vital vehicle for achieving carbon neutrality goals and accelerating the transition to green, low-carbon energy consumption [3,4]. Currently, water electrolysis is the cleanest method for hydrogen production [5], with the main technological pathways categorized into four types: Alkaline Water Electrolysis (AWE) [6–10], Proton Exchange Membrane (PEM) [11–13], Solid Oxide Electrolysis Cells (SOEC) [14,15], and Anion

<sup>\*</sup> Corresponding author. Center for Combustion Energy, Department of Energy and Power Engineering, Key Laboratory for Thermal Science and Power Engineering of Ministry of Education, Low Carbon Energy and CCUS Research Center, Institute for Carbon Neutrality, Tsinghua University, 10084, Beijing, China. E-mail address: k.luo@ucl.ac.uk (K.H. Luo).

Exchange Membrane (AEM) [16–20]. Each of the four water electrolysis technologies presents its own advantages and challenges in terms of materials, performance, efficiency, and cost. Hydrogen production using proton exchange membranes exhibits enhanced resistance to corrosion and functions effectively under reduced cell voltages, increased current densities, and higher pressures [21]. This method provides rapid response capabilities and exceptional load adaptability, rendering it ideal for pairing with renewable energy systems such as photovoltaic and wind power. These energy sources are known for their significant fluctuations and inconsistent availability. [21,22]. Despite their compact design, they are sensitive to water impurities and require expensive materials for durability and conductivity. The porous transport layer (PTL) is essential in optimizing the efficiency and catalyst utilization of PEMWE, thereby contributing to reducing the cost of hydrogen production [23]. Overall, the PEM technology is gaining traction in applications such as automotive hydrogen and fluctuating renewable energy [24].

PEMWEs typically operate at high current densities (greater than 2 A/cm<sup>2</sup>), where oxygen gas accumulation at the anode becomes a major source of performance loss. Generated in the anode catalyst layer (CL), oxygen accumulates in the PTL, leading to three main issues: (1) impeded transport of reactants and products, (2) reduced active area, and (3) poor thermal management [25]. Bubbles trapped in the PTL's pore spaces obstruct mass transport, and the low porosity (30-50 %) of typical titanium PTLs further restricts reactant flow. Increased oxygen saturation exacerbates these limitations, lowering the reaction rate and accelerating the phase transition from dissolved to gaseous oxygen. This results in higher gas phase oxygen content near the electrode and a significant reduction in available active area. Additionally, oxygen's thermal conductivity is lower than that of liquid water, increasing thermal resistance. High current density regions can develop "hotspots" [26,27] where inadequate heat dissipation through cooling or conduction can accelerate membrane degradation. Consequently, addressing the transport issues of oxygen bubbles is crucial for enhancing PEMWE performance.

After bubbles detach from the PTL surface, they disperse within the water flow. At elevated current densities, distinct flow patterns emerge within the flow channel [28]. At lower current densities, bubble coalescence occurs less frequently, resulting in smaller bubbles within the channel. This regime is termed bubbly flow. As the current density increases, bubble coalescence becomes more common, leading to the formation of slug flow, which can occupy the full diameter of the channel, transitioning the flow state to slug flow. With continued gas production, slug flow eventually evolves into annular flow. In this regime, the gas phase occupies a substantial portion of the channel, with water confined to the channel walls. This transition in flow patterns can be observed using a transparent end plate. In a single serpentine flow field, bubbly flow dominates near the inlet, while slug flow appears as water progresses through the channel, and the flow eventually shifts to annular flow in the later sections. Higher current densities not only increase the proportion of slug and annular flow patterns but also accelerate the onset of annular flow [29].

Due to the microscopic and opaque nature of the PTL, it is considered challenging to visually and quantitatively investigate the development and progression of oxygen bubbles within the electrolyzer, as well as the mechanisms of oxygen transport in the PTL. Recent investigations have primarily utilized imaging techniques such as optical microscopy, neutron radiography, X-ray imaging, along with simulation methods. Dedigama et al. [30] and Lee et al. [31] used optical microscopy to examine oxygen transport in PEMWE and microfluidic platforms, enabling them to visualize the behavior of oxygen gas within the electrolyzer. Seweryn et al. [32] and Zlobinski et al. [33] employed neutron radiography to study two-phase flow within the PTLs. Their imaging results indicated that at low current densities, the distribution of oxygen gas remains unaffected by the current density. Selamat et al. [34] employed simultaneous neutron radiography and optical imaging to

visualize two-phase transport in an electrolyzer. X-ray imaging was used by Arbabi et al. [35], Lee et al. [36], Hoeh et al. [37], De Angelis [38], and Kulkarni et al. [39] to investigate the gas transport dynamics within the PTL. Leonard et al. [40] studied the generation and movement of oxygen bubbles using X-ray computed tomography (CT) and radiography. Their findings show that elevated current densities lead to increased oxygen production, followed by faster oxygen bubble detachment. However, it is experimentally challenging to differentiate between water and oxygen for titanium PTLs, due to titanium's X-ray attenuation properties. Therefore, monitoring oxygen in PTLs with X-ray imaging involves expensive and intricate techniques, including the use of appropriate stains, high-resolution optics, and specialized image processing techniques [38], which pose significant challenges for research in this field.

Several theoretical studies have been developed for study of the complex two-phase flows in PTL. Khorasani et al. [41] developed a 1D model to study the growth of the O2 bubbles inside the anodic PTL. Computational approaches have emerged as key tools for addressing multiscale and multiphysics flow challenges, providing essential insights into the two-phase flow dynamics within porous structure. Arbabi et al. [42] developed a three-dimensional, two-phase numerical model using OPENFOAM to simulate oxygen transport in the PTL, employing the Volume of Fluid (VOF) method to accurately capture the gas-liquid interface. The simulation results showed strong agreement with experimental data. Their analysis of oxygen inlet pressure revealed that the critical throat size within the PTL is a crucial factor influencing oxygen transport. Jiang et al. [43] established a 3D, two-phase model for PEMWE which integrates electrochemical reactions, two-phase flow, heat transfer, and hydrogen migration processes. Their study found that optimizing the wettability characteristics of the PTL and CL could significantly improve oxygen expulsion efficiency. Zhou et al. [44] employed the VOF approach to study the development of bubble transport within the PEMWE flow field. Their findings revealed that homogeneous distribution of contact angles in the PTL enhances the mass transfer performance of PEMWE more effectively than gradient distribution. Li et al. [45,46] established a two-dimensional transient VOF model to obtain the detailed gas-liquid interface. Their work focused on the interaction between multiple independent oxygen transport paths. Sun et al. [47] employed the phase field method to precisely capture the two-phase interface and investigated the impact of various structural parameters of the PTL on the dynamics and evolution of liquid water.

One of the pore-scale modelling techniques that has been introduced recently in PEMWE is pore network modelling (PNM) [48]. Vorhauer et al. [49] were among the pioneers in applying PNM to investigate the invasion pattern (IP) of oxygen in the anodic PTL. In a later study, Altaf et al. [50] further expanded on this work by further developing the PNM to explore the invasion pattern at high current densities. Stiber et al. employed a PNM to analyze the mass transport phenomena in PEMWE [51]. The main advantage of PNM lies in its ability to achieve faster simulation times and reduced computational costs [52]. However, PNM simplifies geometric structures and underestimates the impact of critical invasion phenomena, for instance the Haines jumps and capillary valve effect [53].

The lattice Boltzmann method (LBM) has been verified to be an powerful tool for understanding multiphase transport phenomena in porous media, which possesses several advantages over other methods in terms of parallel computational efficiency and ease in treating complex porous structures [54]. Satjaritanun et al. [55] explored the dynamic transport within the PTLs of PEMWE using both X-ray CT and LBM. Their findings showed that the LB model successfully captured the oxygen pattern in the PTL. However, discrepancies were observed between the experimental and simulation results, which were attributed to the LB model's limitations in accurately simulating bubble nucleation and growth. Bhaskaran et al. [56] utilized LBM to analyze the oxygen invasion mechanism in titanium-based PTL, revealing that the spatial

porosity and pore size distribution are key factors governing the final oxygen concentration pattern. Lin et al. [57] presents a numerical simulation study using a 3D pseudopotential multicomponent model to investigate the effects of perforated cracks in the microporous layer of a proton exchange membrane fuel cell on liquid water distribution and flow regime. Jeon et al. [58] explored the motion characteristics of oxygen bubbles in the PTL with a free surface model on the basis of a 3D structure stochastically generated from spherical particles. Their findings indicated that porosity has a significant influence on bubble behavior, whereas the effects of particle radius and PTL thickness were comparatively minor. Paliwal et al. [53] employed LBM to model the oxygen invasion distribution in a water-saturated anode transport layer with a 2D structure, demonstrating that the incorporation of a microporous layer effectively mitigates oxygen accumulation. Lin et al. [59] discussed the influence of contact angle on oxygen transport based on 3D structure of commercial PTLs reconstructed by X-ray tomography. The results indicated that increasing the hydrophilicity reduces oxygen saturation, while simultaneously prolonging the oxygen breakthrough

The existing literature reveals a scarcity of studies focused on the evolution of two-phase flow and bubble transport characteristics within three-dimensional pore-structured PTLs utilizing the LBM.

In the present study, the microscopic transport behaviors of oxygen bubbles within the porous transport layer and flow channel are emphasized. A three-dimensional lattice Boltzmann model with a free surface model was utilized to investigate the invasion of bubbles within PTLs and their flow patterns in the flow channel. Specifically, bubbles will be generated at random positions according to a controllable generation interval in the simulation process, corresponding to the oxygen generation rates at different current densities. The effects of porosity, wettability, initial flow channel velocity and microporous layer structure on bubble transport characteristics were investigated. Additionally, the similarities and differences between sintered and fibrous types of PTLs were revealed. This study aims to enhance the understanding of the mechanisms governing the transport of oxygen bubbles within PTLs and flow channels, providing valuable insights to support the selection and optimization.

### 2. Model development

### 2.1. LBM

The traditional method in CFD involves simulating the evolution of a flow problem through the discretization of the Navier-Stokes equations. Different from this, the LBM is based on solving a discrete form of the Boltzmann equation and has gained popularity in the last few decades. LBM solves the mesoscopic kinetic equation for the particle distribution function (DF)  $f(x,\xi,t)$ , where  $x,\xi,and\,t$  are the phase space, particle velocity space and time [60]. It is well established that the particle velocity space, denoted as  $\xi$ , can be reduced to a finite set of discrete velocities  $\{\xi_i|i=1,...,b\}$ , while maintaining the accuracy of the hydrodynamic moments up to a specified order in  $\xi$  [61].

The lattice Boltzmann equation for adequate space-time discretization is given by:

$$f_i(\mathbf{x} + \mathbf{e}_i \Delta t, t + \Delta t) = f_i(\mathbf{x}, t) - \frac{\Delta t}{\tau} \left[ f_i(\mathbf{x}, t) - f_i^{eq}(\mathbf{x}, t) \right] + \mathbf{F}_i$$
 (1)

where  $e_i$  is the i th lattice velocity vector,  $\tau$  is the relaxation time,  $\Delta t$  is the time step and  $F_i$  is an external force (e.g., gravity). The equilibrium distribution function of the i th discrete velocity is defined as  $f_i^{eq}(\boldsymbol{x},t) = f_i^{eq}(\rho,\mathbf{v})$ , where  $\mathbf{v}$  is velocity and  $\rho$  is density. Eq. (1) is implemented in the BGK approximation, where the collision term is computed using the single relaxation time (SRT) approximation. [62]. The particle velocity space in the fluid is discretized into a set of velocity vectors. In this study, the D3Q19 model is employed, which consists of 19 velocity

vectors in three-dimensional space, as illustrated in Fig. S1.

The equilibrium distribution functions are expressed as detailed

$$f_i^{eq}(\rho, \mathbf{v}) = \rho w_i \left( 1 + 3(\mathbf{e}_i \cdot \mathbf{v}) + \frac{9}{2} (\mathbf{e}_i \cdot \mathbf{v})^2 - \frac{3}{2} \mathbf{v} \cdot \mathbf{v} \right)$$
(2)

where the weights  $w_i$  are 1/3 for i=0,1/18 for i=1,...,6, and 1/36 for i=7,...,18. The macroscopic density  $\rho$  and momentum  $\rho \mathbf{v}$  are calculated as follows:

$$\rho = \sum_{i=0}^{18} f_i \text{ and } \rho \mathbf{v} = \sum_{i=0}^{18} e_i f_i$$
(3)

The basic LBM numerical algorithm is typically split into two steps of collision and streaming as follows:

Collision: 
$$f_i^{out}(\mathbf{x}, t) = f_i^{in}(\mathbf{x}, t) - \frac{1}{\tau} \left[ f_i^{in}(\mathbf{x}, t) - f_i^{eq}(\mathbf{x}, t) \right] + \mathbf{F}_i$$
 (4)

Streaming: 
$$f_i^{in}(\mathbf{x} + \mathbf{e}_i, t + \Delta t) = f_i^{out}(\mathbf{x}, t)$$
 (5)

where  $f_i^{in}$  and  $f_i^{out}$  are the incoming and outgoing DFs. In the collision process Eq. (4), the right-hand side of the equation is the known quantity of the current time step t. In the streaming process Eq. (5), all calculated distribution function but  $f_0$  are transported to their neighboring lattice sites based on their velocity. The sequence in which these two steps are executed is flexible and may differ depending on the implementation in various codes. For example, in WALBERLA, the streaming step is performed first, followed by the collision step. This approach offers the advantage of merging the streaming and collision processes, eliminating the need to store and later retrieve macroscopic values from memory.

The viscosity 
$$\nu$$
 follows from:  $\nu = \frac{1}{3} \left( \tau - \frac{1}{2} \right)$ .

The bounce-back scheme is the most straightforward boundary condition for modeling no-slip obstacles, ensuring zero normal and tangential velocities at the fluid-solid interface. In the streaming step, the DFs are bounced off the obstacle surface [63]; this is mathematically represented by transforming Eq. (5) into (6)

$$f_i^{in}(\mathbf{x}, t + \Delta t) = f_i^{out}(\mathbf{x}, t)$$
(6)

where subscript  $\bar{i}$  refers to the value of the DF in the opposite direction of the corresponding subscript i; thus,  $e_{\bar{i}} = -e_i$ .

### 2.2. The free surface model

The FSLBM enhances the traditional LBM by incorporating a VOF approach [64], where the distinct interface between the two phases is tracked using an indicator field. An extra variable, the volume fraction of fluid  $\varepsilon$ , which represents the proportion of the cell area occupied by fluid, is assigned to each interface cell. The representation of the liquid–gas interface is shown in Fig. S2.

The simulation of free surfaces involves distinguishing fluid-gas regions by designating cells as fluid cells (i.e., containing fluid) or empty cells (i.e., lacking fluid). However, it does not consider the gas part directly, thereby reducing computational complexity in the gas regions. [65]. During the simulation, all cells except obstacle cells can undergo state changes. However, it is important to note that direct transitions between fluid and gas states, and vice versa, are not permitted. Tracing the free surface involves three steps: calculating the interface movement, determining the boundary conditions at the fluid interface, and reinitializing the cell types. The fluid mass content of a cell is represented as  $m(\mathbf{x},t) = \rho(\mathbf{x},t)\varepsilon(\mathbf{x},t)$ , where mass exchange occurs due to the streaming of  $f_i$ . The mass transfer  $\Delta m_i(\mathbf{x},t)$  between an interface cell at lattice site  $\mathbf{x}$  and its neighboring cell in  $\mathbf{e}_i$ -direction at  $\mathbf{x} + \mathbf{e}_i$  is determined as:

$$\Delta m_i(\mathbf{x},t) = \begin{cases} 0 & G \\ f_i^{out}(\mathbf{x}+\mathbf{e}_i,t) - f_i^{out}(\mathbf{x},t) & F \\ \frac{1}{2} \left( \varepsilon(\mathbf{x},t) + \varepsilon(\mathbf{x}+\mathbf{e}_i,t) \right) \left( f_i^{out}(\mathbf{x}+\mathbf{e}_i,t) - f_i^{out}(\mathbf{x},t) \right) & I \end{cases}$$

where G, F and I denote the gas cell, fluid cell, and interface cell, respectively.

The temporal change in the mass content of an interface cell is expressed as follows:

$$m(\mathbf{x}, t + \Delta t) = m(\mathbf{x}, t) + \sum_{i=1}^{b} \Delta m_i(\mathbf{x}, t)$$
(7)

For the boundary conditions at the fluid-gas interface, distribution functions are defined only for fluid and interface cells, while those from gas cells are not specified within the interface cells. As a result, the missing distribution functions are reconstructed as follows:

$$f_i^{\text{out}}(\mathbf{x} - \mathbf{e}_i, t) = f_i^{\text{eq}}(\rho^{\text{G}}, \mathbf{v}) + f_i^{\text{eq}}(\rho^{\text{G}}, \mathbf{v}) - f_i^{\text{out}}(\mathbf{x}, t), \forall i : \mathbf{n} \cdot \mathbf{e}_i \ge 0$$
(8)

where  $\rho^G$  is the gas density and  ${\bf v}$  is the velocity of the interface cell. The influence of surface tension is accounted for through a localized adjustment of the gas pressure:  $p^G(t)=\frac{1}{3}\rho^G(t)-2\kappa(t)\sigma-\Pi$ , where  $\kappa$ ,  $\sigma$  and  $\Pi$  denote the curvature, the surface tension and disjoining pressure, respectively.

#### 2.3. Structure reconstruction

Perforated thin titanium sheets, sintered porous titanium, and titanium fibers constitute the primary types of PTLs. Fig. 1 presents the SEM cross-sectional images and three-dimensional reconstructed geometries of fibrous PTLs and sintered PTLs. Porous media are highly individual, the 2D SEM images were selected to extract the key characteristic geometric features of these two PTL types for 3D structure reconstruction. The porosities selected for the simulation fell within the range in real PTLs. In this work, we constructed the sintered PTL with different

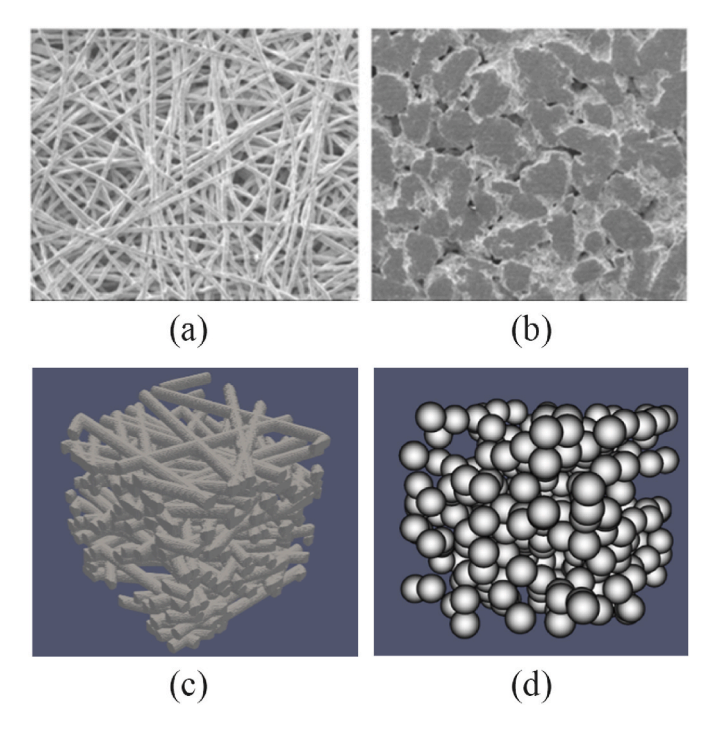


**Fig. 1.** (a) SEM image of fibers PTL; (b) SEM image of sintered porous sinter PTL; (c) 3D reconstructed structure of fiber PTL; (d) 3D reconstructed structure of spherical PTL.

porosities based on the random sphere generation method [58] by adjusting particle diameter and spacing, as commercially fabricated PTLs typically consist of powder-based porous materials with complex microstructures. Solid particles represented the titanium powders with a radius of 20 lu (lu: lattice unit), and void space referred to the pore region characterized by a specific porosity value. For the fibrous PTL, a stochastic generation method [66] was adopted, where the fibers were modeled as randomly arranged cylinders with a predefined diameter, allowing for possible overlap, which reflects the elongated and interwoven characteristics observed in real PTLs. Furthermore, the fibrous PTL with different characteristics was constructed by generating cylinders with a diameter of 20 lu at random position and orientation layer by layer until the required PTL thickness.

#### 2.4. Computational setup

To simulate the whole dynamic process of oxygen bubble transport related to PTL and flow channel, we developed a 3D LB model, as seen in Fig. 2. The model contains a cubical PTL and flow channel with lateral initial velocity in the X direction. The computational domain was selected to be  $300 \times 300 \times 500 \text{ lu}^3$  initially filled with water and a 300 lu PTL thickness was adopted. At the bottom of the domain, corresponding to the catalyst layer, different bubble generation time intervals can be set to add spherical bubbles with a diameter of 20 lu at random positions, corresponding to the oxygen generation rate under different current densities. Spherical bubbles coalesce during their ascent, invade the PTL, and eventually enter the flow channel. The bubble nucleation processes were not considered, and the focus was instead placed on the bubble removal process within the PTL and flow channel. The bounceback scheme was applied to the solid particle surfaces, a no-slip condition was enforced at the top boundary, and periodic boundary conditions were applied at the side boundaries in both the x- and y-directions. All simulations were simulated on ARCHER2 with 45 nodes (128 cores per node).

#### 3. Model validation

We performed rising bubble and Taylor bubble benchmarks to validate our model's capability to simulate fluid-gas behavior. The validation study focused on the ascent of a single bubble driven by buoyancy in an unconfined liquid channel. In the simulation, a gas bubble was initialized as a sphere with a diameter D, positioned at coordinates (4D,4D,1D) within a computational domain of size  $8D\times8D\times4D$ 

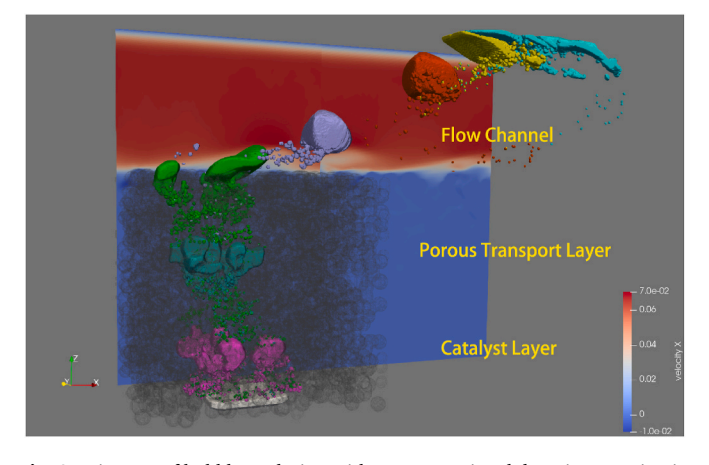


**Fig. 2.** Diagram of bubble evolution with a computational domain extension in the X-direction. Different colored contours represent bubbles at different timestep. The red region in the slice denotes the flow channel, while the gray area represents the porous transport layer. (For interpretation of the references to color in this figure legend, the reader is referred to the Web version of this article.)

(x-,y-,z- direction). Gravity was applied in the negative z-direction. The bubble will eventually stabilize, characterized by a stable upward velocity and equilibrium shape after a certain period of ascent. The simulated bubble shape, shown in Fig. S3, closely matches the experimental results from Reference [67]. Furthermore, the steady-state bubble shapes were found to correspond well with the experimental outcomes, which maintained numerical stability in conditions of high liquid-to-gas density ratio. This demonstrates the qualitative reliability of the current model.

Another test case involves a large gas bubble ascending through a stationary liquid within a confined cylindrical tube, conforming to the experiments in Reference [68]. As the bubble rises, it assumes an elongated form with a rounded front edge. As illustrated in Fig. S6, the computational domain, measuring  $1D \times 1D \times 10D$  (x-,y-,z- direction), represents a cylindrical tube with a diameter of D aligned along the z-axis. A gas bubble was initialized as a cylinder with a diameter of 0.75D and a length of 3D, positioned concentrically within the boundary of the tube. The bottom of the gas bubble was located at a distance of D along the positive z-direction. The computational results capture the interface contour of the bubble moderately well. In Fig. S4, at a radial line situated at 0.504D behind the bubble front, the non-dimensional radial fluid velocity and axial velocity achieved convergence and showed strong agreement with the experimental data. Therefore, the FSLBM model is qualitatively and quantitatively validated using these benchmarks. More verification can be found in Ref. [69].

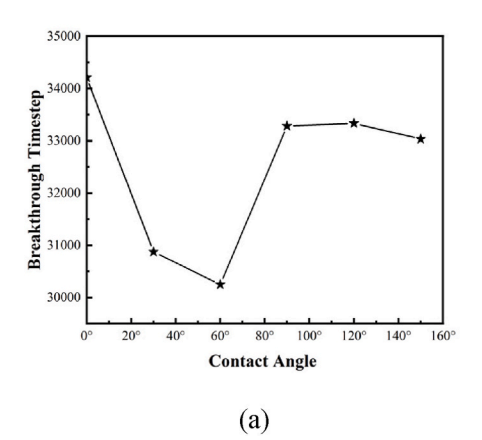
#### 4. Result and discussion

#### 4.1. Bubble transport characteristics in spherical PTLs

Firstly, we define bubble breakthrough time as the time required for gas-labeled cells in the LBM simulation to reach the top plane of the PTL. This represents the time it takes for a gas bubble to travel through the PTL and break through into the flow channel. Fig. S5 illustrates the oxygen transport process and bubble breakthrough time under different bubble generation time intervals. This study differs from previous research in that those studies employed continuous gas injection or preexisting square bubbles, whereas we introduce bubbles from the bottom layer. Continuous gas injection imparts an upward initial velocity to the gas phase, and the square shape of the bubbles is not physically realistic [58]. Therefore, our approach to bubble handling aligns more closely with real-world conditions. It is evident that at shorter generation intervals, particularly when compared to time intervals exceeding 10<sup>2</sup>, the bubble breakthrough time remains relatively constant. As simulation time progresses, oxygen bubbles coalesce during their ascent and do not invade all the pores uniformly. Instead, it selectively moves along

specific pathways, with only a few branches reaching the top of the PTL. This selective pathway choice is primarily attributed to the influence of capillary forces on oxygen transport within the PTL. Driven by capillary forces, oxygen preferentially breaks through pathways with larger throat sizes. However, as the generation interval increases, the time required for bubble breakthrough increases. When the generation intervals are relatively large, oxygen bubbles within the porous transport layer (PTL) exhibit minimal coalescence, rendering the effects of capillary forces nearly negligible. As a result, the bubbles ascend almost independently, leading to a stable breakthrough time. This further underscores the feasibility and necessity of operating PEMWEs under high current density conditions.

To examine the impact of contact angle on oxygen transport, six distinct contact angles were considered, while keeping all other conditions constant. The following equation can describe the capillary pressure in porous structures:  $p_c = 2\sigma \cos \theta / R$ , where  $\sigma$  is the surface tension,  $\theta$  is the contact angle, and R is the pore size. With constant surface tension and pore size, lower capillary pressure corresponds to a larger contact angle. Fig. 3 illustrates the representative oxygen transport process and bubble breakthrough time under different contact angles. Additional breakthrough state under different contact angles can be found in Fig. S6. From the liquid perspective, a smaller contact angle reflects enhanced hydrophilicity of the PTL and increased capillary pressure, whereas from the gas's perspective, it signifies a stronger "repulsive force" exerted by liquid water on the gas. This study shows that hydrophilic PTLs (with contact angles less than 90°) significantly accelerate bubble breakthrough time and more easily facilitate the formation of bubbly flow when the bubbles reach the flow channel. As the contact angle increases, the breakthrough time shortens, primarily due to capillary pressure. When the conditions are hydrophilic, oxygen behaves as the non-wetting phase, where capillary pressure hinders its movement. As the hydrophilicity increases, the resistance to oxygen transport also increases, as described by the equation of capillary pressure. Hence, as the contact angle increases, the time required for oxygen breakthrough decreases. An optimal contact angle is likely around 60°. The results are generally consistent with previous experimental studies [70]. Oxygen typically moves through capillary fingering, involving a breakthrough event where oxygen surmounts the capillary resistance at the pore throat. As a result, oxygen preferentially penetrates pores that have the lowest capillary resistance. Under conditions of higher hydrophilicity, the elevated capillary resistance limits oxygen movement to a few pathways containing larger pores. Conversely, with an increase in the contact angle, the capillary resistance at pores of equivalent size diminishes, facilitating greater oxygen penetration into more pores. This results in a more uniform distribution of bubbles within the PTL, enabling them to ascend into the flow channel through multiple



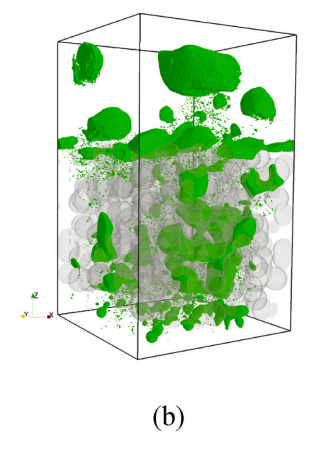
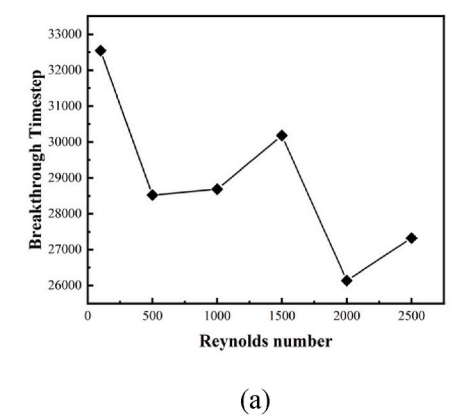


Fig. 3. (a) Bubble breakthrough timestep of different contact angles (b) Oxygen distribution of PTL with contact angle  $= 60^{\circ}$ . The transparent part of the computational domain represents the liquid phase, the gray parts represent the porous transport layer, and the green parts represent oxygen. (For interpretation of the references to color in this figure legend, the reader is referred to the Web version of this article.)

pathways, thereby approaching the desired bubble flow regime. In the hydrophilic regime, capillary forces act as resistance, limiting bubbles to propagate along larger pores and leading to faster breakthrough. In contrast, under hydrophobic conditions, capillary forces switch to a driver role, causing bubbles to occupy more pores, which slows down the longitudinal breakthrough process. For hydrophobic PTLs, the bubble breakthrough time is longer and exhibits minimal variation, and bubbles are more prone to coalesce and develop into slug flow, oxygen transport is governed by capillary pressure, which drives it into pores with varying throat sizes. Instead of capillary fingering, the movement transitions to a stable displacement mode, aligning with the model described in the literature [71]. The above analysis successfully explains why the bubble breakthrough time remains relatively constant under hydrophobic conditions, with a slight decrease observed as the contact angle increases. Once the bubbles reach the flow channel, they are more prone to coalescence, although they remain more dispersed than when the capillary pressure is zero (at a contact angle of 90°).

Fig. 4 illustrates the representative oxygen transport process and bubble breakthrough time at varying initial flow channel Reynolds numbers. Additional breakthrough state under different Reynolds numbers can be found in Fig. S7. This study demonstrates that an increase in Reynolds number accelerates the bubble expulsion process. At lower flow velocities, ascending bubbles within the channel are more likely to reach the top of the computational domain, where the no-slip boundary condition at the top impedes bubble movement within the flow channel. This situation favors the formation of slug flow. Conversely, when the initial Reynolds number exceeds 2000, conditions become more conducive to suppressing slug bubble formation, leading to a reduced separation diameter and enhanced mass transfer within the PEMWE. The stress analysis diagram illustrating the detachment of oxygen bubbles from the PTL is presented in Fig. S8. Influenced by the interplay of various forces, oxygen bubbles progress through three distinct phases: growth, migration, and detachment within the flow channel. Finally, they are carried out of the electrolysis cell by the entraining action of liquid water within the flow channel. From the stress analysis perspective, an increase in flow velocity within the channel generates greater drag forces exerted by the flowing liquid water on the bubbles, thereby facilitating their detachment from the PTL/flow channel interface. Consequently, the size of the bubbles within the channel decreases, promoting the establishment of a bubble flow regime. If the flow velocity continues to increase, it may transition into turbulent flow, which can result in a slight increase in breakthrough time. However, flow velocity cannot be excessively high due to constraints imposed by operating conditions, reactant supply and demand, energy consumption, and other factors.



# 4.2. Comparison of bubble transport characteristics between fibrous PTL and spherical PTL

This section aims to systematically analyze the differences between fibrous and spherical PTLs under high current density conditions. Fig. 5 presents the comparison of breakthrough time and gas spatial saturation for fibrous and spherical PTLs with the same porosity, under bubble generation time intervals of 10 and 50 time steps. The diameters of the spherical particles and cylindrical fibers are both 10 lu, and the two types of PTLs share the same porosity of 63.5 %. For spherical PTLs, decreasing the generation interval further under higher generation rates does not accelerate breakthrough time; instead, it slows down. This occurs because the increased branching of tree-like bubbles within the pores complicates lateral movement, resulting in delayed discharge and a greater likelihood of bubbles remaining trapped in the PTL, thereby affecting the two-phase mass transfer process on the anode side. For fibrous PTLs, further shortening the generation interval accelerates the bubble breakthrough process, and the residual bubbles near the catalyst layer are fewer compared to those in spherical PTLs. For both types of PTLs, further reducing the bubble generation interval results in an increase in the detachment bubble size into the flow channel. Compared to fibrous PTLs, the geometric structure of spherical PTLs is also more prone to the formation of slug flow. In general, PEMWEs operate at higher current densities, resulting in a faster hydrogen production rate. From the above comparisons, we can conclude that fibrous PTLs are more suitable for high-current density operations.

# 4.3. Comparison of bubble transport characteristics between graded porosity fibrous PTLs

Fig. 6 compares the bubble breakthrough time and spatial distribution of gas saturation for high-to-low and low-to-high porosity gradient PTLs (from the catalyst layer to the flow channel), with a reference porosity of 63.5 %. In the figure, the time is expressed as a percentage of the breakthrough time relative to that of the reference porosity. In comparison to sintered PTLs, layer-by-layer fabricated fibrous PTLs are more amenable to processing into features with graded porosity. We configured two types of fibrous PTLs with porosity gradients ranging from 45 % to 75 % and from 75 % to 45 % (from the catalyst layer to the flow channel). Three-dimensional structures are presented in Fig. S9. Similar to the water saturation analysis method in Reference [57], the oxygen saturation analysis was conducted along the height of the PTL. The bubble breakthrough time for low-to-high porosity gradient PTL does not show significant differences compared to high-to-low porosity gradient PTL. However, it is evident that the accumulation of bubbles in the middle of the PTL is noticeably reduced. Larger pore spaces may

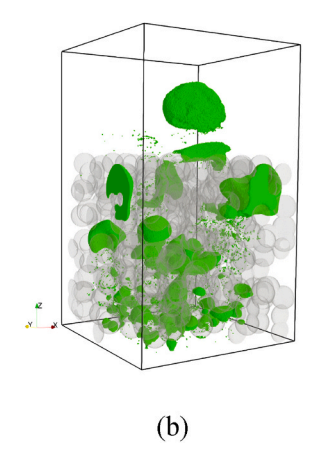


**Fig. 4.** (a) Bubble breakthrough timestep of different Reynolds numbers (b) Oxygen distribution of PTL with Reynolds number = 2500. The transparent part of the computational domain represents the liquid phase, the gray parts represent the porous transport layer, and the green parts represent oxygen. (For interpretation of the references to color in this figure legend, the reader is referred to the Web version of this article.)

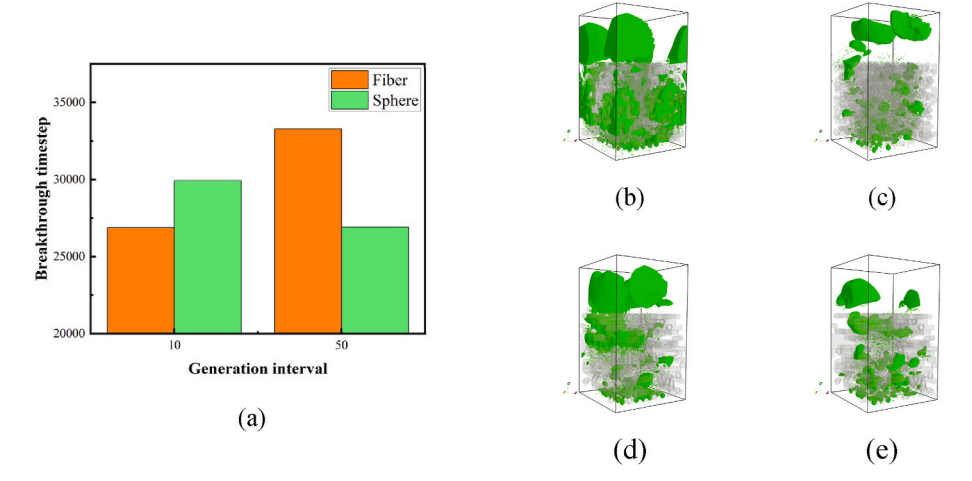
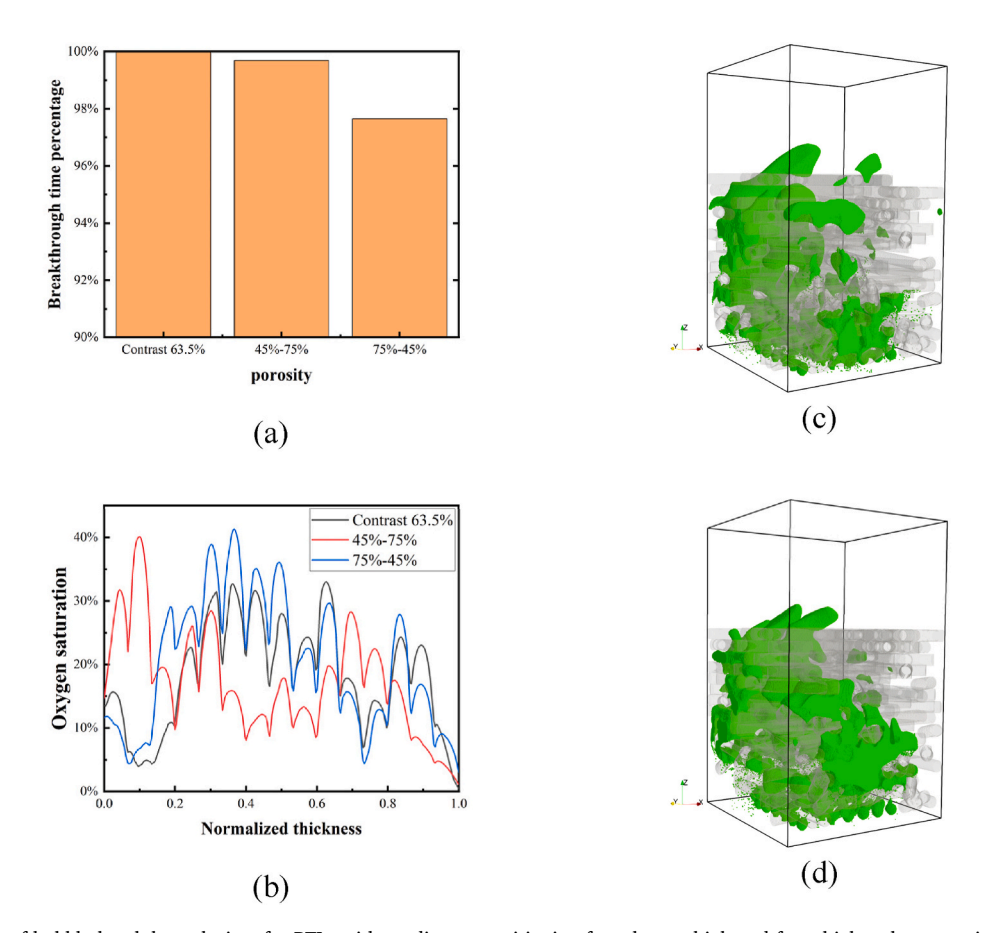


Fig. 5. (a) Comparison of breakthrough time for fibrous and spherical PTLs with the same porosity (b) Oxygen distribution for spherical PTL with interval = 10 (c) Oxygen distribution for spherical PTL with interval = 50 (d) Oxygen distribution for fibrous PTL with interval = 10 (e) Oxygen distribution for fibrous PTL with interval = 50. The transparent part of the computational domain represents the liquid phase, the gray parts represent the porous transport layer, and the green parts represent oxygen. (For interpretation of the references to color in this figure legend, the reader is referred to the Web version of this article.)



**Fig. 6.** (a) Comparison of bubble breakthrough time for PTLs with gradients transitioning from low to high and from high to low porosity (b) Oxygen saturation distribution along the normalized thickness of different PTLs at breakthrough time (c) Gas saturation distribution for 45 %–75 % (d) Gas saturation distribution for 75 %–45 %. The transparent part of the computational domain represents the liquid phase, the gray parts represent the porous transport layer, and the green parts represent oxygen. (For interpretation of the references to color in this figure legend, the reader is referred to the Web version of this article.)

offer bubbles a faster upward migration, leading to a slightly shorter breakthrough time compared to the control group. For low-to-high porosity gradient PTL, the upper layer features larger pore throat sizes, enabling oxygen to merge into larger bubbles. The gradual reduced capillary resistance in this region also facilitates the entry of bubbles with larger detachment diameters into the flow channel, making

slug flow formation more likely. Compared to the control, the gas saturation in the middle of the PTL is lower. In the bottommost layer where gas infiltrates, the rapid bubble generation combined with limited porosity leads to a localized region of elevated gas saturation, which quickly diminishes. For high-to-low porosity gradient PTL, the lower layer provides larger pore spaces, where bubbles accumulate after

coalescing during their ascent. As the porosity decreases along the height, the density of the fibers increases, leading to higher capillary resistance, which makes the bubble breakthrough process to the upper layers more challenging. The gas saturation in the middle layer of the PTL significantly increases, thereby hindering the heat and mass transfer processes. In summary, the selection and manufacture of PTLs should carefully balance the effects of gradient porosity on bubble detachment diameter and gas spatial saturation. Building on these findings, the next section explores how modifications in fiber diameter, rather than porosity, influence bubble transport characteristics in PTLs.

# 4.4. Effects of microporous layer structure on bubble transport characteristics

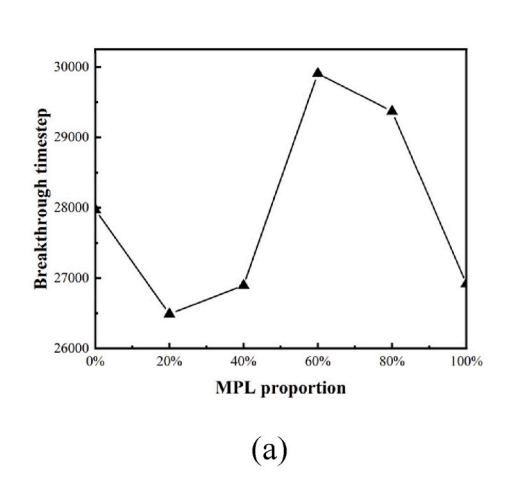
While Section 4.3 focused on the effects of graded porosity, this section explores the effects of changing fiber diameters under constant porosity conditions. Both sections contribute to a comprehensive understanding of how varying structural parameters affect bubble transport in PTLs. Fig. 7 presents the bubble breakthrough time and gas saturation spatial distribution for spherical PTLs with different proportions of microporous layer. For spherical PTLs, we first provide an explanation of the microporous layer configuration. The basic form of the PTL consists of particles with a diameter of 20 lu, while a group of particles with a uniform diameter of 10 lu is positioned at the bottom to serve as the microporous layer. Importantly, both the upper layer (with 20 lu particles) and the lower layer (with 10 lu particles) maintain the same porosity, ensuring a consistent overall porosity distribution throughout the PTL structure. The proportion of the microporous layer is defined by the height of the 10 lu particle group relative to the overall height of the PTL. Smaller diameter fibers are utilized on the side adjacent to the catalyst layer to promote reaction uniformity, minimize resistance, and enable the efficient expulsion of oxygen. In contrast, larger diameter fibers are employed on the side near the flow channel to widen the throat, thereby decreasing oxygen transport resistance. This study indicates that the presence of a small proportion of the microporous layer can effectively accelerate bubble expulsion. However, as the proportion of the microporous layer increases, changes in pore size and flow pathways lead to a transformation in the shape and size of bubble

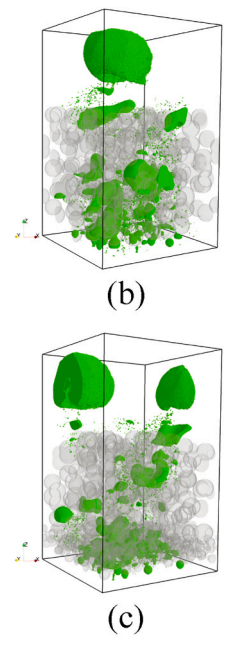
clusters from a clumped distribution to a branched distribution. This enhanced lateral diffusion consequently slows down the bubble expulsion process. For PTLs with global diameters of 20 lu and 10 lu, it was found that a smaller diameter corresponds to an earlier breakthrough time and a lower saturation in the dynamic equilibrium state. However, under constant porosity conditions, decreasing the fiber diameter increases the fiber density and reduces the average pore throat width, thereby enhancing capillary resistance.

Fig. 8 illustrates the impact of a microporous layer (MPL) on the transport characteristics of fibrous PTLs with varying porosities. For fibrous PTLs, the diameter of the fibers in the bottom four layers is set to half that of the fibers in the upper section, functioning as a microporous layer, as seen in Fig. S10. In the case of fibrous PTLs, the presence of a microporous layer, similar to that in spherical PTLs, reduces the accumulation of oxygen near the catalyst layer (CL). However, unlike spherical PTLs, it does not accelerate the ascent of bubbles. Increased lateral movement consumes more time, particularly as porosity decreases and fiber density increases, which further prolongs the time required for lateral movement. Additionally, the incorporation of a microporous layer can effectively reduce the bubble detachment diameter into flow channel. The comparison reveals that while higher porosity facilitates the expulsion of oxygen, it simultaneously reduces the contact area between the PTL and the catalyst layer, potentially impacting efficiency. This presents a dual influence on the two-phase transport within PEMWE.

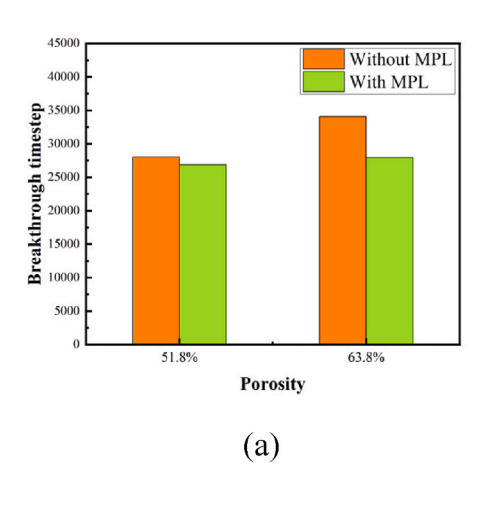
#### 5. Conclusion

In this work, we study the oxygen bubble evolutionary characteristics in the porous transport layer and flow channel of a PEMWE. The 3D geometries of sintered and fibrous PTLs were reconstructed based on randomly distributed spherical particles and layer-by-layer generated cylindrical fibers, respectively. At the bottom of the domain, corresponding to the catalyst layer, different bubble generation time intervals are set to add spherical bubbles at random positions, corresponding to the oxygen generation rate under different current densities. The 3D two-phase bubble flow dynamics within the PTL and flow channel was simulated using a new pore-scale lattice Boltzmann model with a free





**Fig. 7.** (a) Bubble breakthrough timestep of different MPL proportions (b) Oxygen distribution of spherical PTL without MPL (c) Oxygen distribution of spherical PTL with 20 % MPL at porosity = 63.5 %. The transparent part of the computational domain represents the liquid phase, the gray parts represent the porous transport layer, and the green parts represent oxygen. (For interpretation of the references to color in this figure legend, the reader is referred to the Web version of this article.)



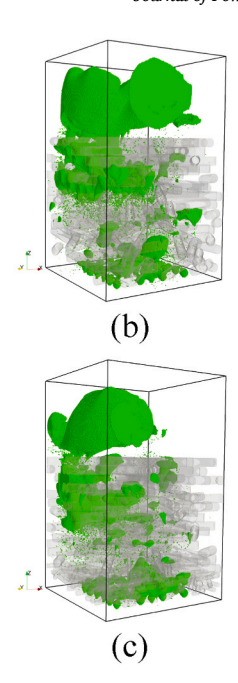


**Fig. 8.** (a) The effects of MPL on breakthrough timestep of fibrous PTLs with varying porosities (b) Oxygen distribution of fibrous PTL without MPL at porosity = 63.5 % (c) Oxygen distribution of fibrous PTL with MPL at porosity = 63.5 %. The transparent part of the computational domain represents the liquid phase, the gray parts represent the porous transport layer, and the green parts represent oxygen. (For interpretation of the references to color in this figure legend, the reader is referred to the Web version of this article.)

surface model. This study explores the oxygen transport characteristics in the PTL and flow channel, focusing on the effects of bubble generation time interval, contact angle of porous media, initial flow velocity, graded porosity and microporous layer structure. It also investigates the differences caused by spherical and fibrous PTLs. The key conclusions can be summarized as follows.

- (1) The breakthrough time for bubbles generated at shorter time intervals is significantly less than that for longer intervals, with smaller variations observed at shorter generation intervals. This further underscores the feasibility and necessity of operating PEMWEs at high current densities.
- (2) Compared to the stable displacement bubble movement pattern in hydrophobic PTLs, hydrophilic PTLs are more conducive to the bubble expulsion process. Under the hydrophilic condition, the larger contact angle accelerates the bubble breakthrough time and facilitates bubbly flow pattern in the flow channel, with an optimal contact angle around 60°. Increasing the velocity in the flow channel can enhance bubble expulsion. However, the transition from laminar to turbulent flow may counteract this effect.
- (3) Unlike spherical PTLs, further reducing the bubble generation time interval leads to faster breakthrough times and less bubble accumulation within the pore spaces for fibrous PTLs. Therefore, fibrous PTLs are more suitable for operation at high current densities.
- (4) For low-to-high porosity (from the catalyst layer to the flow channel) gradient fibrous PTLs, the accumulation of bubbles near the catalyst layer side is significantly reduced. The gradual reduced capillary resistance along the height also facilitates larger bubble detachment diameters into the flow channel, making slug flow formation more likely.
- (5) Microporous layer structure affects gas saturation spatial distribution and mass transport. The presence of a microporous layer efficiently reduces the accumulation of oxygen near the catalyst layer side. In terms of breakthrough time, the microporous layer facilitates the performance of spherical PTLs, while it has the opposite effect on fibrous PTLs.

#### CRediT authorship contribution statement

Ziheng Ding: Writing – original draft, Visualization, Validation, Methodology, Investigation, Formal analysis, Conceptualization. Ruixin Li: Writing – original draft, Investigation. Kai H. Luo: Writing – review & editing, Writing – original draft, Supervision, Funding acquisition, Formal analysis, Conceptualization.

# Declaration of competing interest

The authors declare that they have no known competing financial interests or personal relationships that could have appeared to influence the work reported in this paper.

# Acknowledgement

The research is supported by the Carbon Neutrality and Energy System Transformation (CNEST) Program led by Tsinghua University. Funding for the supercomputing time on ARCHER2 from the UK Engineering and Physical Sciences Research Council under the project "UK Consortium on Mesoscale Engineering Sciences (UKCOMES)" (Grant No. EP/X035875/1) is also acknowledged. This work made use of computational support by CoSeC, the Computational Science Centre for Research Communities, through UKCOMES.

#### Appendix B. Supplementary data

Supplementary data to this article can be found online at https://doi.org/10.1016/j.jpowsour.2025.236959.

#### Appendix A. Supplementary data

Supplementary data to this article can be found online at.

# Data availability

The authors do not have permission to share data.

#### References

- [1] L. Chen, G. Msigwa, M. Yang, A.I. Osman, S. Fawzy, D.W. Rooney, P.-S. Yap, Strategies to achieve a carbon neutral society: a review, Environ. Chem. Lett. 20 (2022) 2277–2310, https://doi.org/10.1007/s10311-022-01435-8.
- [2] Z. Liu, Y. Sun, C. Xing, J. Liu, Y. He, Y. Zhou, G. Zhang, Artificial intelligence powered large-scale renewable integrations in multi-energy systems for carbon neutrality transition: challenges and future perspectives, Energy AI 10 (2022) 100195, https://doi.org/10.1016/j.egyai.2022.100195.
- [3] K. Ayers, N. Danilovic, R. Ouimet, M. Carmo, B. Pivovar, M. Bornstein, Perspectives on low-temperature electrolysis and potential for renewable hydrogen at scale, Annu. Rev. Chem. Biomol. Eng. 10 (2019) 219–239, https://doi.org/10.1146/ annurev-chembioeng-060718-030241.
- [4] T. Capurso, M. Stefanizzi, M. Torresi, S.M. Camporeale, Perspective of the role of hydrogen in the 21st century energy transition, Energy Convers. Manag. 251 (2022) 114898. https://doi.org/10.1016/j.enconman.2021.114898.
- [5] M. El-Shafie, Hydrogen production by water electrolysis technologies: a review, Res Eng 20 (2023) 101426, https://doi.org/10.1016/j.rineng.2023.101426.
- [6] D.M.F. Santos, C.A.C. Sequeira, J.L. Figueiredo, Hydrogen production by alkaline water electrolysis, Quim. Nova 36 (2013). https://doi.org/10.1590/S0100-404220 13000800017.
- [7] S. Marini, P. Salvi, P. Nelli, R. Pesenti, M. Villa, M. Berrettoni, G. Zangari, Y. Kiros, Advanced alkaline water electrolysis, Electrochim. Acta 82 (2012) 384–391, https://doi.org/10.1016/j.electacta.2012.05.011.
- [8] A. Manabe, M. Kashiwase, T. Hashimoto, T. Hayashida, A. Kato, K. Hirao, I. Shimomura, I. Nagashima, Basic study of alkaline water electrolysis, Electrochim. Acta 100 (2013) 249–256, https://doi.org/10.1016/j.electacta.2012.12.105
- [9] M. Rashid, M. Al Mesfer, H. Naseem, Danish, hydrogen production by water electrolysis: a review of alkaline water electrolysis, PEM water electrolysis and high temperature water electrolysis, Int. J. Eng. Adv. Technol. (2015) 2249–8958.
- [10] K. Zeng, D. Zhang, Recent progress in alkaline water electrolysis for hydrogen production and applications, Prog. Energy Combust. Sci. 36 (2010) 307–326, https://doi.org/10.1016/j.pecs.2009.11.002.
- [11] M. Carmo, D.L. Fritz, J. Mergel, D. Stolten, A comprehensive review on PEM water electrolysis, Int. J. Hydrogen Energy 38 (2013) 4901–4934, https://doi.org/ 10.1016/j.ijhydene.2013.01.151.
- [12] M. Langemann, D.L. Fritz, M. Müller, D. Stolten, Validation and characterization of suitable materials for bipolar plates in PEM water electrolysis, Int. J. Hydrogen Energy 40 (2015) 11385–11391, https://doi.org/10.1016/j.ijhydene.2015.04.155.
- [13] T. Smolinka, S.E. Ise, PEM Water Electrolysis-Present Status of Research and Development, Review Lecture, 2010.
- [14] Y. Zheng, J. Wang, B. Yu, W. Zhang, J. Chen, J. Qiao, J. Zhang, A review of high temperature co-electrolysis of H2O and CO2 to produce sustainable fuels using solid oxide electrolysis cells (SOECs): advanced materials and technology, Chem. Soc. Rev. 46 (2017) 1427–1463, https://doi.org/10.1039/C6CS00403B.
- [15] S.E. Wolf, F.E. Winterhalder, V. Vibhu, L.G.J. de Haart, O. Guillon, R.-A. Eichel, N. H. Menzler, Solid oxide electrolysis cells current material development and industrial application, J. Mater. Chem. A 11 (2023) 17977–18028, https://doi.org/10.1039/D3TA02161K
- [16] M. Faraj, E. Elia, M. Boccia, A. Filpi, A. Pucci, F. Ciardelli, New anion conducting membranes based on functionalized styrene-butadiene-styrene triblock copolymer for fuel cells applications, J. Polym. Sci. Polym. Chem. 49 (2011) 3437–3447, https://doi.org/10.1002/pola.24781.
- [17] A. Filpi, M. Boccia, H. Gasteiger, Pt-free cathode catalyst performance in H2/O2 anion-exchange membrane fuel cells (AMFCs), ECS Trans 16 (2008) 1835. https://doi.org/10.1149/1.2982024.
- [18] M. Piana, S. Catanorchi, H.A. Gasteiger, Kinetics of non-platinum group metal catalysts for the oxygen reduction reaction in alkaline medium, ECS Trans. 16 (2008) 2045, https://doi.org/10.1149/1.2982044.
- [19] M. Piana, M. Boccia, A. Filpi, E. Flammia, H.A. Miller, M. Orsini, F. Salusti, S. Santiccioli, F. Ciardelli, A. Pucci, H2/air alkaline membrane fuel cell performance and durability, using novel ionomer and non-platinum group metal cathode catalyst, J. Power Sources 195 (2010) 5875–5881, https://doi.org/ 10.1016/j.jpowsour.2009.12.085.
- [20] I. Vincent, D. Bessarabov, Low cost hydrogen production by anion exchange membrane electrolysis: a review, Renew. Sustain. Energy Rev. 81 (2018) 1690–1704, https://doi.org/10.1016/j.rser.2017.05.258.
- [21] S. Shiva Kumar, V. Himabindu, Hydrogen production by PEM water electrolysis a review, Mater Sci Energy Technol 2 (2019) 442–454, https://doi.org/10.1016/j. prest 2010.03.002
- [22] Y. Wang, Y. Pang, H. Xu, A. Martinez, K.S. Chen, PEM Fuel cell and electrolysis cell technologies and hydrogen infrastructure development – a review, Energy Environ. Sci. 15 (2022) 2288–2328, https://doi.org/10.1039/D2EE00790H.
- [23] M. Maier, K. Smith, J. Dodwell, G. Hinds, P.R. Shearing, D.J.L. Brett, Mass transport in PEM water electrolysers: a review, Int. J. Hydrogen Energy 47 (2022) 30–56, https://doi.org/10.1016/j.ijhydene.2021.10.013.
- [24] S. Yuan, C. Zhao, X. Čai, L. An, S. Shen, X. Yan, J. Zhang, Bubble evolution and transport in PEM water electrolysis: mechanism, impact, and management, Prog. Energy Combust. Sci. 96 (2023) 101075, https://doi.org/10.1016/j. pecs.2023.101075.
- [25] C.H. Lee, R. Banerjee, F. Arbabi, J. Hinebaugh, A. Bazylak, in: ASME 2016 14th International Conference on Nanochannels, Microchannels, and Minichannels Collocated with the ASME 2016 Heat Transfer Summer Conference and the ASME 2016 Fluids Engineering Division Summer Meeting, 2016.

- [26] P. Millet, A. Ranjbari, F. de Guglielmo, S.A. Grigoriev, F. Auprêtre, Cell failure mechanisms in PEM water electrolyzers, Int. J. Hydrogen Energy 37 (2012) 17478–17487, https://doi.org/10.1016/j.ijhydene.2012.06.017.
- [27] S. Sun, Y. Xiao, D. Liang, Z. Shao, H. Yu, M. Hou, B. Yi, Behaviors of a proton exchange membrane electrolyzer under water starvation, RSC Adv. 5 (2015) 14506–14513, https://doi.org/10.1039/C4RA14104K.
- [28] W. Wang, S. Yu, K. Li, L. Ding, Z. Xie, Y. Li, G. Yang, D.A. Cullen, H. Yu, Z. Kang, J. A. Wrubel, Z. Ma, G. Bender, C.B. Capuano, A. Keane, F.-Y. Zhang, Insights into the rapid two-phase transport dynamics in different structured porous transport layers of water electrolyzers through high-speed visualization, J. Power Sources 516 (2021) 230641, https://doi.org/10.1016/j.jpowsour.2021.230641.
- [29] J.O. Majasan, J.I.S. Cho, I. Dedigama, D. Tsaoulidis, P. Shearing, D.J.L. Brett, Two-phase flow behaviour and performance of polymer electrolyte membrane electrolysers: electrochemical and optical characterisation, Int. J. Hydrogen Energy 43 (2018) 15659–15672, https://doi.org/10.1016/j.ijhydene.2018.07.003.
- [30] I. Dedigama, P. Angeli, N. van Dijk, J. Millichamp, D. Tsaoulidis, P.R. Shearing, D. J.L. Brett, Current density mapping and optical flow visualisation of a polymer electrolyte membrane water electrolyser, J. Power Sources 265 (2014) 97–103, https://doi.org/10.1016/j.jpowsour.2014.04.120.
- [31] C. Lee, J. Hinebaugh, R. Banerjee, S. Chevalier, R. Abouatallah, R. Wang, A. Bazylak, Influence of limiting throat and flow regime on oxygen bubble saturation of polymer electrolyte membrane electrolyzer porous transport layers, Int. J. Hydrogen Energy 42 (2017) 2724–2735, https://doi.org/10.1016/j. ijhydene.2016.09.114.
- [32] J. Seweryn, J. Biesdorf, T.J. Schmidt, P. Boillat, Communication—neutron radiography of the water/gas distribution in the porous layers of an operating electrolyser, J. Electrochem. Soc. 163 (2016) F3009, https://doi.org/10.1149/ 2.0641607jes.
- [33] M. Zlobinski, T. Schuler, F.N. Büchi, T.J. Schmidt, P. Boillat, Transient and steady state two-phase flow in anodic porous transport layer of proton exchange membrane water electrolyzer, J. Electrochem. Soc. 167 (2020) 084509, https:// doi.org/10.1149/1945-7111/ab8c89.
- [34] O.F. Selamet, U. Pasaogullari, D. Spernjak, D.S. Hussey, D.L. Jacobson, M.D. Mat, Two-phase flow in a proton exchange membrane electrolyzer visualized in situ by simultaneous neutron radiography and optical imaging, Int. J. Hydrogen Energy 38 (2013) 5823–5835, https://doi.org/10.1016/j.jihydene.2013.02.087.
- [35] F. Arbabi, A. Kalantarian, R. Abouatallah, R. Wang, J.S. Wallace, A. Bazylak, Feasibility study of using microfluidic platforms for visualizing bubble flows in electrolyzer gas diffusion layers, J. Power Sources 258 (2014) 142–149, https:// doi.org/10.1016/i.jpowsour.2014.02.042.
- [36] C.H. Lee, J.K. Lee, B. Zhao, K.F. Fahy, A. Bazylak, Transient gas distribution in porous transport layers of polymer electrolyte membrane electrolyzers, J. Electrochem. Soc. 167 (2020) 024508, https://doi.org/10.1149/1945-7111/ https://doi.org/10.1149/1945-7111/
- [37] M.A. Hoeh, T. Arlt, I. Manke, J. Banhart, D.L. Fritz, W. Maier, W. Lehnert, In operando synchrotron X-ray radiography studies of polymer electrolyte membrane water electrolyzers, Electrochem. Commun. 55 (2015) 55–59, https://doi.org/10.1016/j.elecom.2015.03.009.
- [38] S. De Angelis, T. Schuler, M.A. Charalambous, F. Marone, T.J. Schmidt, F.N. Büchi, Unraveling two-phase transport in porous transport layer materials for polymer electrolyte water electrolysis, J. Mater. Chem. A 9 (2021) 22102–22113, https://doi.org/10.1039/D1TA03379D.
- [39] D. Kulkarni, A. Huynh, P. Satjaritanun, M. O'Brien, S. Shimpalee, D. Parkinson, P. Shevchenko, F. DeCarlo, N. Danilovic, K.E. Ayers, C. Capuano, I.V. Zenyuk, Elucidating effects of catalyst loadings and porous transport layer morphologies on operation of proton exchange membrane water electrolyzers, Appl. Catal. B Environ. 308 (2022) 121213, https://doi.org/10.1016/j.apcatb.2022.121213.
- [40] E. Leonard, A.D. Shum, S. Normile, D.C. Sabarirajan, D.G. Yared, X. Xiao, I. V. Zenyuk, Operando X-ray tomography and sub-second radiography for characterizing transport in polymer electrolyte membrane electrolyzer, Electrochim. Acta 276 (2018) 424–433, https://doi.org/10.1016/j.electacta.2018, 04.144.
- [41] A. Nouri-Khorasani, E. Tabu Ojong, T. Smolinka, D.P. Wilkinson, Model of oxygen bubbles and performance impact in the porous transport layer of PEM water electrolysis cells, Int. J. Hydrogen Energy 42 (2017) 28665–28680, https://doi. org/10.1016/j.ijhydene.2017.09.167.
- [42] F. Arbabi, H. Montazeri, R. Abouatallah, R. Wang, A. Bazylak, Three-dimensional computational fluid dynamics modelling of oxygen bubble transport in polymer electrolyte membrane electrolyzer porous transport layers, J. Electrochem. Soc. 163 (2016) F3062, https://doi.org/10.1149/2.0091611jes.
- [43] Y. Jiang, Y. Li, Y. Ding, S. Hu, J. Dang, F. Yang, M. Ouyang, Simulation and experiment study on two-phase flow characteristics of proton exchange membrane electrolysis cell, J. Power Sources 553 (2023) 232303, https://doi.org/10.1016/j. ipowsour 2022 232303
- [44] H. Zhou, K. Meng, W. Chen, B. Chen, Two-phase flow evolution and bubble transport characteristics in flow field of proton exchange membrane water electrolyzer based on volume of fluid-coupled electrochemical method, J. Clean. Prod. 425 (2023) 138988, https://doi.org/10.1016/j.jclepro.2023.138988.
- [45] Q. Li, C. Bao, Z. Jiang, X. Zhang, T. Ding, C. Fang, M. Ouyang, Numerical study on oxygen transport pattern in porous transport layer of proton exchange membrane electrolysis cells, eTransportation 15 (2023) 100210, https://doi.org/10.1016/j. etran.2022.100210.
- [46] Q. Li, C. Bao, Z. Li, Z. Jiang, X. Zhang, Two-dimensional numerical pore-scale investigation of oxygen evolution in proton exchange membrane electrolysis cells, Int. J. Hydrogen Energy 47 (2022) 16335–16346, https://doi.org/10.1016/j. ijhydene.2022.03.156.

- [47] Y. Sun, C. Bao, Z. Jiang, X. Zhang, T. Gao, A two-dimensional numerical study of liquid water breakthrough in gas diffusion layer based on phase field method, J. Power Sources 448 (2020) 227352, https://doi.org/10.1016/j. ipowsour.2019.227352.
- [48] J.K. Lee, C.H. Lee, A. Bazylak, Pore network modelling to enhance liquid water transport through porous transport layers for polymer electrolyte membrane electrolyzers, J. Power Sources 437 (2019) 226910, https://doi.org/10.1016/j. jpowsour.2019.226910.
- [49] N. Vorhauer, H. Altaf, E. Tsotsas, T. Vidakovic-Koch, Pore Network Simulation of Gas-Liquid Distribution in Porous Transport Layers, Processes 7 (9) (2019) 558. https://doi.org/10.3390/pr7090558.
- [50] H. Altaf, N. Vorhauer, E. Tsotsas, T. Vidaković-Koch, Steady-State Water Drainage by Oxygen in Anodic Porous Transport Layer of Electrolyzers: A 2D Pore Network Study, Processes 8 (3) (2020) 362. https://doi.org/10.3390/pr7090558.
- [51] S. Stiber, N. Sata, T. Morawietz, S.A. Ansar, T. Jahnke, J.K. Lee, A. Bazylak, A. Fallisch, A.S. Gago, K.A. Friedrich, A high-performance, durable and low-cost proton exchange membrane electrolyser with stainless steel components, Energy Environ. Sci. 15 (2022) 109–122, https://doi.org/10.1039/D1EE02112E.
- [52] S. Jung, M. Sabharwal, A. Jarauta, F. Wei, M. Gingras, J. Gostick, M. Secanell, Estimation of relative transport properties in porous transport layers using porescale and pore-network simulations, J. Electrochem. Soc. 168 (2021) 064501, https://doi.org/10.1149/1945-7111/ac03f2.
- [53] S. Paliwal, D. Panda, S. Bhaskaran, N. Vorhauer-Huget, E. Tsotsas, V.K. Surasani, Lattice Boltzmann method to study the water-oxygen distributions in porous transport layer (PTL) of polymer electrolyte membrane (PEM) electrolyser, Int. J. Hydrogen Energy 46 (2021) 22747–22762, https://doi.org/10.1016/j. iihydene.2021.04.112.
- [54] Q. Li, K.H. Luo, Q.J. Kang, Y.L. He, Q. Chen, Q. Liu, Lattice Boltzmann methods for multiphase flow and phase-change heat transfer, Prog. Energy Combust. Sci. 52 (2016) 62–105, https://doi.org/10.1016/j.pecs.2015.10.001.
- [55] P. Satjaritanun, M. O'Brien, D. Kulkarni, S. Shimpalee, C. Capuano, K.E. Ayers, N. Danilovic, D.Y. Parkinson, I.V. Zenyuk, Observation of preferential pathways for oxygen removal through porous transport layers of polymer electrolyte water electrolyzers, iScience 23 (2020) 101783, https://doi.org/10.1016/j. isci.2020.101783.
- [56] S. Bhaskaran, D. Pandey, V.K. Surasani, E. Tsotsas, T. Vidakovic-Koch, N. Vorhauer-Huget, LBM studies at pore scale for graded anodic porous transport layer (PTL) of PEM water electrolyzer, Int. J. Hydrogen Energy 47 (2022) 31551–31565, https://doi.org/10.1016/j.ijhydene.2022.07.079.
- [57] R. Lin, M. Dong, S. Lan, M. Lou, Numerical simulation of liquid water transport in perforated cracks of microporous layer, Energy 262 (2023) 125372, https://doi. org/10.1016/j.energy.2022.125372.
- [58] D.H. Jeon, S. Kim, M. Kim, C. Lee, H.-S. Cho, Oxygen bubble transport in a porous transport layer of polymer electrolyte water electrolyzer, J. Power Sources 553 (2023) 232322, https://doi.org/10.1016/j.jpowsour.2022.232322.

- [59] R. Lin, J. Huo, X. Cai, S. Lan, Z. Hao, Numerical study of the effects of wettability and hierarchical porosity on oxygen transport within the porous transport layer of proton exchange membrane electrolyzers, J. Power Sources 614 (2024) 235030, https://doi.org/10.1016/j.jpowsour.2024.235030.
- [60] C. Körner, M. Thies, T. Hofmann, N. Thürey, U. Rüde, Lattice Boltzmann model for free surface flow for modeling foaming, J. Stat. Phys. 121 (2005) 179–196, https:// doi.org/10.1007/s10955-005-8879-8.
- [61] X. He, L.-S. Luo, Theory of the lattice Boltzmann method: from the Boltzmann equation to the lattice Boltzmann equation, Phys. Rev. 56 (1997) 6811–6817, https://doi.org/10.1103/PhysRevE.56.6811.
- [62] P.L. Bhatnagar, E.P. Gross, M. Krook, A model for collision processes in gases. I. Small amplitude processes in charged and neutral one-component systems, Phys. Rev. 94 (1954) 511–525, https://doi.org/10.1103/PhysRev.94.511.
- [63] N. Thürey, U. Rüde, Stable free surface flows with the lattice Boltzmann method on adaptively coarsened grids, Comput. Visual Sci. 12 (2009) 247–263, https://doi. org/10.1007/s00791-008-0090-4.
- [64] C.W. Hirt, B.D. Nichols, Volume of fluid (VOF) method for the dynamics of free boundaries, J. Comput. Phys. 39 (1981) 201–225, https://doi.org/10.1016/0021-9991(81)90145-5.
- [65] N. Thürey, U. Rüde, Stable free surface flows with the lattice Boltzmann method on adaptively coarsened grids, Comput. Visual Sci. 12 (2009) 247–263. https://doi. org/10.1007/s00791-008-0090-4.
- [66] L. Hao, P. Cheng, Lattice Boltzmann simulations of water transport in gas diffusion layer of a polymer electrolyte membrane fuel cell, J. Power Sources 195 (2010) 3870–3881, https://doi.org/10.1016/j.jpowsour.2009.11.125.
- [67] D. Bhaga, M.E. Weber, Bubbles in viscous liquids: shapes, wakes and velocities, J. Fluid Mech. 105 (1981) 61–85, https://doi.org/10.1017/S002211208100311X.
- [68] J. Bugg, G. Saad, The velocity field around a Taylor bubble rising in a stagnant viscous fluid: numerical and experimental results, Int. J. Multiphas. Flow 28 (2002) 791–803. https://doi.org/10.1016/S0301-9322(02)00002-2.
- [69] C. Schwarzmeier, M. Holzer, T. Mitchell, M. Lehmann, F. Häusl, U. Rüde, Comparison of free-surface and conservative Allen–Cahn phase-field lattice Boltzmann method, J. Comput. Phys. 473 (2023) 111753, https://doi.org/ 10.1016/j.jcp.2022.111753.
- [70] A. Zinser, G. Papakonstantinou, K. Sundmacher, Analysis of mass transport processes in the anodic porous transport layer in PEM water electrolysers, Int. J. Hydrogen Energy 44 (2019) 28077–28087, https://doi.org/10.1016/j. ijhydene.2019.09.081.
- [71] L. Jianxin, L. Zongqi, Z. Xiaolei, H. Gulizhaina, C. Xuedi, Wettability and wettability modification methods of porous transport layer in polymer electrolyte membrane electrolysis cells (PEMEC): a review, Int. J. Hydrogen Energy 48 (2023) 26629–26651, https://doi.org/10.1016/j.ijhydene.2023.03.409.